

Achieving increased resolution and reconstructed image quality with gradient variance modified super-resolution radial fluctuations

Xingyu Gong

Fudan University

Li Zhou

Fudan University

Longfang Yao

Fudan University

Li Zhang

Fudan University

Liwen Chen

Fudan University

Yiyan Fei

Fudan University <https://orcid.org/0000-0002-2413-130X>

Lan Mi

Fudan University <https://orcid.org/0000-0002-2320-2225>

Baoju Wang

South China Normal University

Jiong Ma (✉ jjiongma@fudan.edu.cn)

Fudan University

Article

Keywords: Degree of Gradient Convergence, Temporal Fluctuation Analysis, Localization Microscopy Methods, Artifacts and Background Noise

Posted Date: July 2nd, 2021

DOI: <https://doi.org/10.21203/rs.3.rs-608461/v1>

License:   This work is licensed under a Creative Commons Attribution 4.0 International License.

[Read Full License](#)

1 **Achieving increased resolution and reconstructed image quality with gradient**
2 **variance modified super-resolution radial fluctuations**

3
4 Xingyu Gong ^{1,5}, Li Zhou ^{2,5}, Longfang Yao ¹, Li Zhang ², Liwen Chen ¹, Yiyan Fei ¹, Lan Mi ¹,
5 *, Baoju Wang ^{3,*} and Jiong Ma ^{1,2,4,*}

6
7 ¹ Department of Optical Science and Engineering, Shanghai Engineering Research Center of Ultra-
8 precision Optical Manufacturing, Key Laboratory of Micro and Nano Photonic Structures (Ministry
9 of Education), Green Photoelectron Platform, Fudan University, 220 Handan Road, Shanghai
10 200433, China.

11 ² Shanghai Engineering Research Center of Industrial Microorganisms, The Multiscale Research
12 Institute of Complex Systems (MRICS), School of Life Sciences, Fudan University, 220 Handan
13 Road, Shanghai 200433, China

14 ³ Centre for Optical and Electromagnetic Research, Guangdong Provincial Key Laboratory of
15 Optical Information Materials and Technology, South China Academy of Advanced Optoelectronics,
16 South China Normal University, Guangzhou 510006, China.

17 ⁴ Institute of Biomedical Engineering and Technology, Academy for Engineer and Technology,
18 Fudan University, 220 Handan Road, Shanghai 200433, China

19 ⁵ These authors contributed equally: Xingyu Gong and Li Zhou

20 * email: lanmi@fudan.edu.cn; baoju.wang@m.scnu.edu.cn; jiongma@fudan.edu.cn

21
22 **Abstract**

23 Based on the calculation of the degree of gradient convergence, the super-
24 resolution radial fluctuations (SRRF) algorithm can achieve higher resolution by
25 combining temporal fluctuation analysis with localization microscopy methods. The
26 algorithm is also capable of processing high-density fluorescence images. However,
27 there are considerable artifacts due to high density, which lead to a loss of image
28 resolution and low fidelity of images. This study demonstrates the use of fluorescence
29 gradient fluctuations in super-resolution analysis and proposes gradient variance
30 modified SRRF (gmSRRF) algorithm. The gmSRRF algorithm resolves finer structures
31 and compensates for the loss of resolution caused by artifacts in SRRF images using
32 relatively high-density stochastic optical reconstruction microscopy (STORM) data and
33 conventional widefield, confocal, or structured illumination microscopy (SIM) imaging

34 sequences. The effectiveness of this algorithm is proven by means of relevant
35 simulations and experiments, which allow the reconstructed SRRF image to improve
36 resolution and reduce artifacts and background noise.

37

38 **Introduction**

39 In the last two decades, optical super-resolution imaging techniques have made
40 rapid and significant progress. The theoretical diffraction limit has been overcome using
41 several well-established techniques. One of these techniques is single-molecule
42 localization microscopy (SMLM), which is based on the detection of a single molecule¹
43 and typically includes stochastic optical reconstruction microscopy (STORM)^{2, 3} and
44 photoactivated localization microscopy (PALM)^{4, 5}. Other approaches include
45 stimulated emission depletion (STED) microscopy^{6, 7} and structured illumination
46 microscopy (SIM)^{8, 9}, known as point spread function (PSF) modulation techniques.
47 STORM and PALM need a great deal of time for super-resolution imaging, and the
48 samples require complicated preparation. Faster reconstruction algorithms for SIM
49 have been demonstrated^{10, 11}, and STED can be used for dynamic live-cell imaging^{12, 13}.
50 However, their resolutions are relatively inferior to those of STORM and PALM
51 imaging. SIM and PALM also require stable and precise microscopy systems and
52 complex setups.

53 Fluorescence signal processing methods with faster and simplified systems have
54 recently emerged. Typical algorithms include the Bayesian analysis of blinking and
55 bleaching (3B)¹⁴, super-resolution optical fluctuation imaging (SOFI)¹⁵ and super-

56 resolution radial fluctuations (SRRF)¹⁶. 3B can reach a resolution of ~50 nm, but
57 requires a large amount of calculation. For example, 6 h were required to analyze a 1.5
58 × 1.5 μm region¹⁴. SOFI can achieve a resolution of ~150 nm, but requires thousands
59 of frames. Although SRRF has achieved approximately 105 nm for widefield and 80–
60 98 nm for confocal microscopy data using hundreds of slides or less¹⁶, high-density
61 fluorescence signals will cause artifacts and decrease the actual resolution of the SRRF
62 images.

63 Here, we present a gradient variance modified SRRF algorithm (gmSRRF) that
64 addresses artifacts by combining SRRF with the temporal statistics analysis of intensity
65 and gradient fluctuations. The optimization algorithm was verified using stimulated and
66 experimental data. Compared with the SRRF algorithm, the gmSRRF algorithm was
67 proven to achieve better super-resolution reconstructed images with fewer artifacts
68 caused by high density and background noise. Additionally, it was applicable to
69 widefield and confocal data.

70

71 **Algorithm and simulation sections**

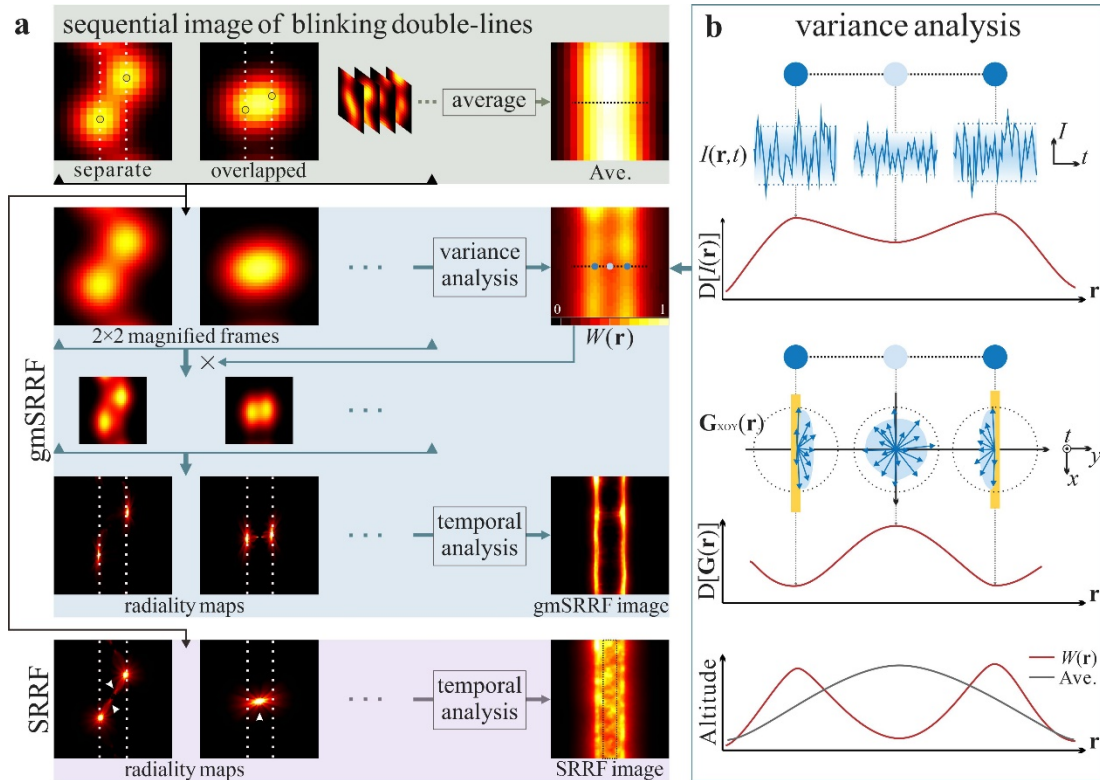
72 There is a conflict between the density of activated fluorophores per frame and the
73 necessary number of frames needed to reconstruct a complete image. SMLM requires
74 low density data for high precision localization, so many frames are needed. SRRF is a
75 super-resolution algorithm that does not depend on the sparse distribution of excited
76 fluorophores¹⁷. Thus, it can achieve super-resolution with fewer frames than SMLM. It
77 calculates the degree of local gradient convergence (radiality) of an image sequence

78 and combines the radiality stack into one reconstructed image through temporal
79 analysis on a sub-pixel scale¹⁸. SRRF also interpolates the images by a factor of
80 “magnification” before processing. However, for high-density data in areas where
81 structures are close and complex, two or more fluorophores can overlap so that the
82 calculated radiality stack cannot achieve multi-center of radiality. This results in
83 artifacts or even misinterpretation of biological structures in reconstructed images, as
84 shown at the bottom of Fig. 1a. These artifacts cannot be depressed by increasing the
85 number of frames. Fewer frames are necessary to compose a super-resolution image
86 using SRRF if artifacts produced during the processing of high-density data are reduced.

87 Modifying raw data is a feasible way to erase artifacts in SRRF images.
88 Temporally dynamic pixel values in a sequence of fluorescence images contain two
89 major parameters of labeled structures, intensity and gradient, denoted by $U(\mathbf{r},t)$ and
90 $\mathbf{G}(\mathbf{r},t)$, respectively. The SRRF algorithm uses radiality to approach intensity peaks
91 without changing the original physical size of the PSF. Thus, its high resolution is based
92 on separate PSFs, which are invalid in high-density situations. The essential issue is
93 resolve two overlapping fluorophores but not to shrink the PSF of an already resolvable
94 fluorophore. SRRF significantly improves the contrast of the images on the basis of the
95 corresponding resolution of exclusive methods, which is exactly the resolution limit of
96 SRRF. While SOFI has demonstrated intensity fluctuations, cumulants can shrink the
97 size of the PSF¹⁵ without depending on the detection and localization of isolated
98 fluorophores, as is the case for STORM^{19,20}. The time-varying concept can be extended
99 to a gradient when the three conditions adopted by SOFI are met. Through deduction,

100 the time-varying properties of the two major parameters are highly related to the
 101 location of \mathbf{r} in relation to a real fluorescence emitter. Specifically, if \mathbf{r} is located
 102 between two close fluorophores:

- 103 1. The corresponding $U(\mathbf{r},t)$ is the sum of the two individual stochastic fluctuations,
 104 which fluctuates less than that of a single molecule because of the averaging effect.
- 105 2. The gradient vector exhibits a higher variety of orientation and amplitude than at
 106 the center of either fluorophore, due to blinking on both sides.



107
 108 **Fig. 1 a** Principle of the gmSRRF algorithm and mechanism of artifacts in SRRF when
 109 processing a simulated image sequence of a vertical double-line structure labeled with
 110 high blinking ratio fluorophores. **b** Progress of variance analysis using three typical
 111 pixel points as examples. The top graph represents the time-varying intensity and its
 112 variance curve. The middle graph is a schematic diagram of projections of gradient
 113 vectors in every moment (blue arrows) on the XOY plane and its variance curve. Yellow
 114 bars indicate the actual position of the double-lines. The bottom graph shows the curves
 115 of weighting function and average intensity.

116

117 In more general cases, a sample is composed of N single-blinking fluorophores.

118 The intensity distribution function is expressed as:

$$119 \quad U(\mathbf{r}, t) = \sum_i^N U(\mathbf{r} - \mathbf{r}_i) a_i f_i(t), \quad (1)$$

120 where $U(\mathbf{r})$ is the point spread function, a_i is the maximum brightness of the
 121 fluorophores, and $f_i(t)$ is the blinking function, assumed to stochastically range between
 122 0 and 1.

123 Variance is used as a quantitative indicator to describe the time-varying properties of
 124 $\mathbf{G}(\mathbf{r}, t)$ and $U(\mathbf{r}, t)$. Here, the variance is equivalent to the concept of zero-time lag
 125 second-order auto-cumulant²¹. The intensity variance is expressed as:

$$\begin{aligned} D[I(\mathbf{r})] &= \langle (U(\mathbf{r}, t) - \langle U(\mathbf{r}, t) \rangle)^2 \rangle_t \\ &= \langle (\sum_i^N U(\mathbf{r} - \mathbf{r}_i) a_i \delta f_i(t))^2 \rangle_t \\ &= \sum_i^N U(\mathbf{r} - \mathbf{r}_i)^2 a_i^2 \langle \delta f_i(t) \rangle_t^2 \\ &= \sum_i^N U(\mathbf{r} - \mathbf{r}_i)^2 a_i^2 D[f_i(t)] \end{aligned} \quad (2)$$

126 where $\delta f_i(t) = f_i(t) - \langle f_i(t) \rangle_t$ and $D[X]$ denotes the variance of time series X .

128 Fluorophores blink relatively independently, so the time average of the cross-terms is
 129 $\langle \delta f_i(t) \delta f_j(t) \rangle_t \neq 0$ only when $i = j$.

130 Subsequently, we use a Gaussian PSF, and the gradients can be expressed as:

$$131 \quad G_x(\mathbf{r}, t) = -\frac{(x - x_i)}{\sigma^2} U(\mathbf{r}, t), \quad (3)$$

$$132 \quad G_y(\mathbf{r}, t) = -\frac{(y - y_i)}{\sigma^2} U(\mathbf{r}, t). \quad (4)$$

133 Following the same simplification method, gradient variance can then be expressed as:

$$\begin{aligned} D[\mathbf{G}(\mathbf{r})] &= D[\mathbf{G}_x(\mathbf{r}, t)] + D[\mathbf{G}_y(\mathbf{r}, t)] \\ &= \sum_i^N \frac{|\mathbf{r} - \mathbf{r}_i|^2}{\sigma^4} U(\mathbf{r} - \mathbf{r}_i)^2 a_i^2 D[f_i(t)] \end{aligned} \quad (5)$$

135 According to the spatial features of the variances of $\mathbf{G}(\mathbf{r}, t)$ and $U(\mathbf{r}, t)$, we define the

136 intensity weighting function at position \mathbf{r} as:

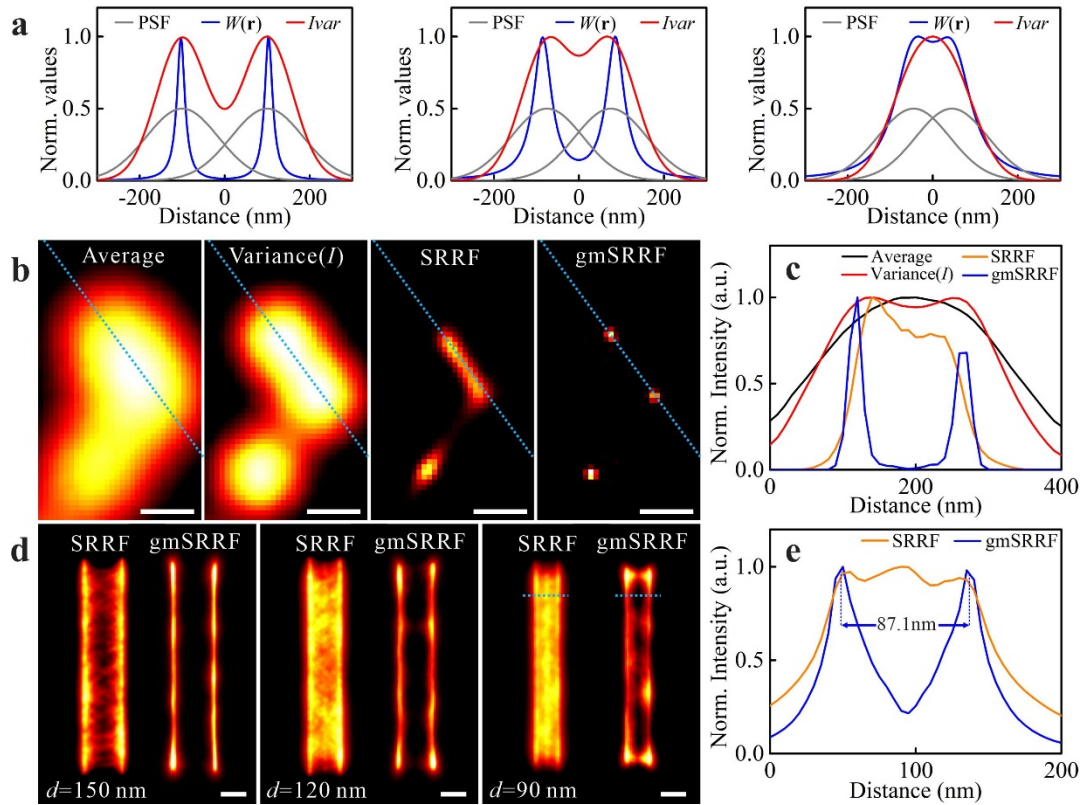
$$W(\mathbf{r}) = \frac{D[I(\mathbf{r})]}{D[\mathbf{G}(\mathbf{r})]}. \quad (6)$$

137
138 The intensity weighting function $W(\mathbf{r})$ describes how the gradient variance and
139 intensity variance vary with positions relative to the center of the real PSF. As
140 mentioned above, the numerator reduces and denominator increases if \mathbf{r} is located
141 between two close fluorophores. A low $W(\mathbf{r})$ indicates non-center. When fluorophores
142 fluctuate with the same statistical characteristics, $a_i \approx a_j$, $D[f_i(t)] \approx D[f_j(t)]$, and
143 $W(\mathbf{r})$ approximates to a sum of impulse functions. However, this approximation is less
144 precise when the fluorescence signal density increases. The $W(\mathbf{r})$ profile is calculated
145 to improve the resolution of the two overlapping blinking PSFs by a factor of
146 $2\sqrt{2\log_3 2}$ (≈ 2.2) compared to the PSF profile (Supplementary Text 1). The $W(\mathbf{r})$
147 profile can better resolve two overlapping PSFs. Therefore, the radially maps have
148 fewer artifacts if the gradient vector fields of raw image sequence are modified by the
149 $W(\mathbf{r})$ profile. Therefore, we present gmSRRF, which calculates $W(\mathbf{r})$ based on 2×2
150 magnified pixels for more precision and fewer interpolation errors, as shown in the
151 middle of Fig. 1a. Subsequently, the reweighted sequence $W(\mathbf{r})U(\mathbf{r},t)$ is processed with
152 SRRF instead of the original $U(\mathbf{r},t)$ sequence. All simulations and experiments follow
153 these same rules:

- 154 1. SRRF alone performs 6 times magnification.
- 155 2. gmSRRF distributes two times magnification for calculation of the weighting
156 function and three times magnification for SRRF analysis; thus, the total
157 magnification is also 6.

158

159 The Monte Carlo method was used to plot the $W(\mathbf{r})$ and intensity variance (I_{var})
160 across two blinking PSFs with different spacings, as shown in Fig. 2a. The full-width
161 half-maximum (FWHM) of the simulated Gaussian PSF was set to 200 nm. The $W(\mathbf{r})$
162 profile showed two resolved peaks when the spacing of the two PSFs was 90 nm, which
163 indicates an approximately 2.2 times improvement in the aspect of spatial resolution.
164 Then, the discrete blinking points were simulated and the image sequence was
165 processed by the SRRF and gmSRRF algorithms. A comparison of the four
166 reconstructed images is shown in Fig. 2b, which indicates that the gmSRRF algorithm
167 has an excellent ability to resolve overlapping molecules. Simulated images of double-
168 lines with different distances (d) were also processed, as seen in Fig. 2d. The gmSRRF
169 images were cleaner with fewer artifacts than the corresponding SRRF images for
170 relatively large spacing ($d = 150$ or 120 nm). When the double-lines were close to 90
171 nm, simple SRRF reconstruction processing caused many artifacts, as shown in Fig. 2d.
172 At the same time, the profile of the intensity section also revealed an unveracious peak
173 between the double-lines, as seen in Fig. 2e. In contrast, the gmSRRF algorithm reduced
174 artifacts and maintained high fidelity and higher resolution of the reconstructed images.



175

176 **Fig. 2** Simulations of the gmSRRF algorithm. In all simulations, the FWHM of the
 177 Gaussian PSF was 200 nm. **a** From left to right: the $W(\mathbf{r})$ and intensity variance (I_{var})
 178 profiles of two simulated blinking PSFs are 200, 150, and 90 nm apart. Gray lines
 179 indicate the positions of the two PSFs. **b** Comparison of simulated blinking discrete
 180 single molecule sequences processed with different methods. From left to right: average
 181 intensity, intensity variance, SRRF, and gmSRRF. Scale bars: 100 nm. **c** The profile of
 182 **b**. **d** Comparison of double-line image sequences processed with SRRF and gmSRRF.
 183 Scale bars: 100 nm. **e** The profile of resolved double-lines with a 90 nm space.

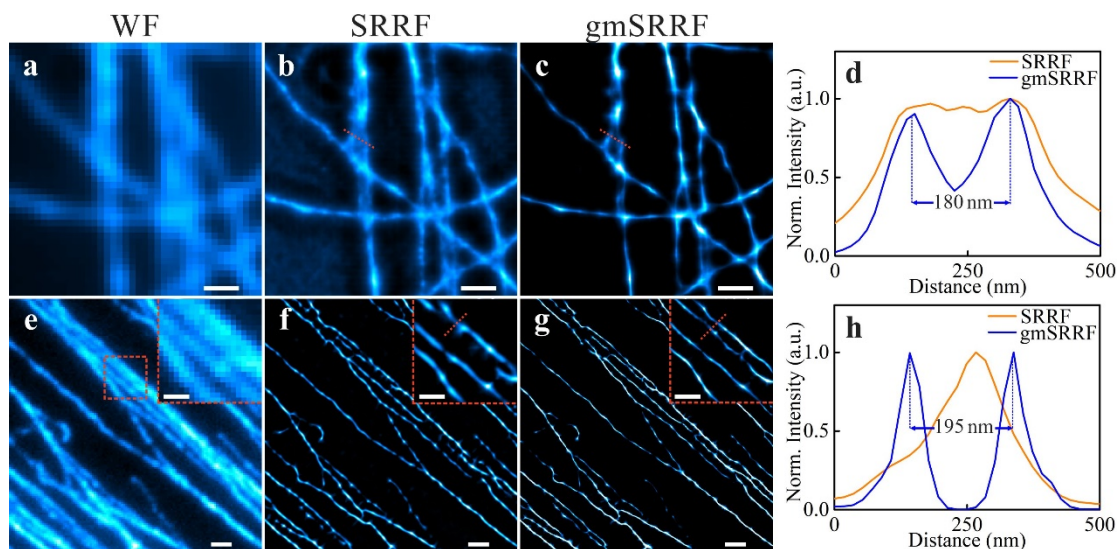
184

185 Experimental section

186 The gmSRRF algorithm was tested on images from high-density STORM data to
 187 verify the practical effectiveness of reducing artifacts originating from high density.
 188 The algorithm was also applied to widefield, confocal, and SIM data to research the
 189 scale of applicability.

190 First, to verify the effectiveness of the gmSRRF algorithm in terms of eliminating
 191 artifacts, high-density STORM raw data were downloaded from the EPFL website²².

192 SRRF and gmSRRF were applied to the data and the reconstructed images are shown
 193 in Figs. 3b and c, respectively. The gmSRRF image shows a distinct bimodal profile
 194 for two close microtubules, as seen in Fig. 3d, while the SRRF image suffered from
 195 bright artifacts and background noise. The labeling density was then set to be extremely
 196 high, creating widefield imaging. An Olympus IX83 inverted microscope was used to
 197 acquire widefield images of the microtubules, which were labeled with Alexa Fluor 488
 198 by immunofluorescence staining in fixed BSC-1 cells. The gmSRRF image resolved
 199 more microtubule structures, which were missing in the SRRF image, as shown in Figs.
 200 3f and g, respectively. The SRRF algorithm failed to resolve the parallel microtubules
 201 shown in the red dashed box because the bright side overpowered the dim side in
 202 intensity.



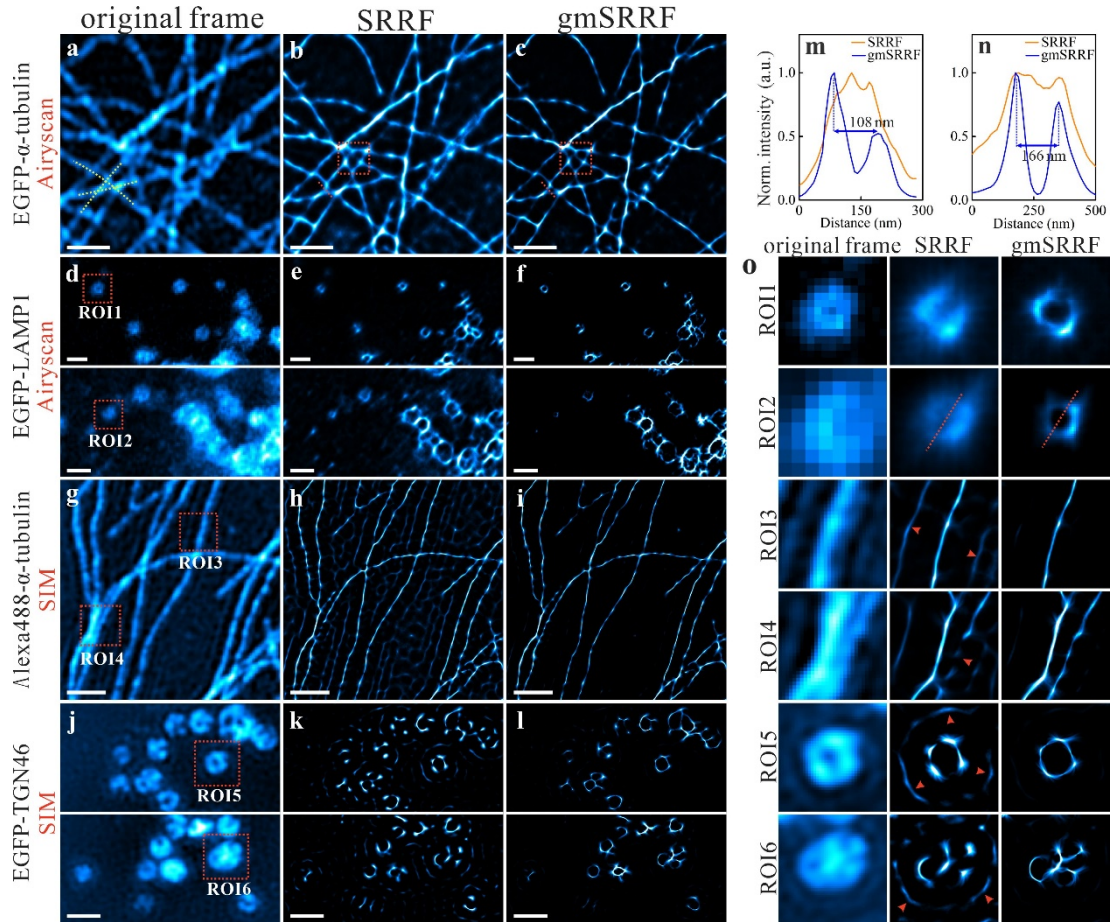
203
 204 **Fig. 3** Comparison of SRRF and gmSRRF under different imaging conditions, such as
 205 high-density STORM data and widefield data. **a** Average image of STORM data served
 206 as widefield imaging. **b** and **c** STORM data was processed with SRRF and gmSRRF
 207 algorithms, respectively. **d** Profiles along the red dotted lines in **b** and **c**. **e** Widefield
 208 image of subcellular microtubules. **f** and **g** Widefield images processed with the SRRF
 209 and gmSRRF algorithms, respectively. **h** Profiles along the red dotted lines in **f** and **g**.
 210 For **a-c**: Scale bar is 500 nm. For **e-g**: Scale bar is 1 μm for full view and 500 nm for
 211 region of interest (ROI).

212

213 Sequential data acquired with a confocal microscope were also processed by SRRF
214 and improved by the gmSRRF algorithm. Airyscan microscopy from ZEISS can
215 increase the lateral resolution and signal-to-noise ratio (SNR) of the traditional laser
216 scanning confocal microscope²³. Therefore, we used a ZEISS Airyscan microscope
217 LSM880 for confocal imaging. α -tubulin tagged with enhanced green fluorescent
218 protein (EGFP) could denote microtubules as a representative linear structure sample.
219 The confocal image, and reconstructed SRRF and gmSRRF images are shown in Figs.
220 4a-c, respectively. SRRF produced a Y-shaped misinterpreted structure for the
221 triangular structures, as shown in Fig. 4a. gmSRRF produced a correct profile of the
222 crossing structures, as shown in Fig. 4m. In addition, the lysosome images of Airyscan
223 were acquired. Therefore, the application of the gmSRRF algorithm revealed a number
224 of individual lysosomes that were not well interpreted by the SRRF algorithm, as shown
225 in Figs. 4d-f.

226 Han et al. applied the SRRF algorithm to 9-frames of raw SIM data and obtained
227 an improved resolution compared with the SIM algorithm²⁴. However, 9 frames are
228 inadequate for a high-SNR image. SIM image sequences are accessible for SRRF
229 processing because fast SIM acquisition is already well-established. Therefore,
230 sequential SIM acquisition was adopted in the experimental design. The reduction of
231 SIM artifacts and revelation of hidden structures were proven in microtubule sequential
232 images acquired with SIM, as seen in Figs. 4g-i. The ring-shaped *trans*-Golgi
233 subcellular structures were also imaged sequentially by SIM for further comparison
234 analysis, and the results are shown in Figs. 4j-l. The phenomenon of loss and

235 discontinuity of continuous structures existed in the SRRF image because of uneven
236 fluorescent intensity. In contrast, the gmSRRF image delivered more continuous
237 structures. In addition, SIM images showed considerable pseudo structures around the
238 true cell structures and in the background, as seen in Figs. 4g and j, respectively. The
239 artifacts became more severe after processing with the SRRF algorithm. These high-
240 frequency pseudo-patterns caused by raw data intensity issues are commonly seen
241 reconstruction artifacts in SIM^{25, 26}. Several algorithms have been proposed to address
242 sidelobe artifacts and improve calculations in the frequency domain^{27, 28}. gmSRRF
243 appeared to be functional for SIM artifacts in the spatial-temporal domain, filtering out
244 the residual noise signal before it produced artifacts. This is because SIM artifacts
245 exhibit a low stochastic variation in intensity and a relatively high variation in gradient.
246



247

248 **Fig. 4** Resolution and imaging quality improvement in Airyscan images and SIM
 249 images. **a** Airyscan image of microtubules. Yellow dotted lines show a triangular
 250 structure formed by three crossing microtubules. **b** and **c** Corresponding SRRF and
 251 gmSRRF reconstructed images, respectively. **d** Airyscan sequence images of lysosomes
 252 marked by EGFP-LAMP1. The entire field of view was composed of two different
 253 regions. **e** and **f** Corresponding SRRF and gmSRRF reconstructed images, respectively.
 254 **g** SIM sequence of microtubules marked by Alexa Fluor 488. **h** and **i** Corresponding
 255 SRRF and gmSRRF reconstructed images, respectively. **j** SIM sequence of *trans*-Golgi
 256 marked by EGFP-TGN46. The entire field of view was composed of two different
 257 regions. **k** and **l** Corresponding SRRF and gmSRRF reconstructed images, respectively.
 258 **m** The profiles along the red dotted lines in **b** and **c**. **n** The profiles along the red dotted
 259 lines in the detailed SRRF and gmSRRF images in ROI2. **o** The magnified details of
 260 the original SRRF and gmSRRF frames, labeled with ROI1-6. Scale bars: 1 μ m.

261

262 Conclusion

263 This study proposed an improved gmSRRF algorithm based on fluorescence
 264 fluctuations and blinking that analyzed the intensity variance and gradient variance of

265 raw sequential data to calculate the weighting function used for pre-processing. The
266 proposed gmSRRF algorithm could depress the false radial center accumulated in
267 SRRF processing to deal with artifacts caused by high density. Additionally, two-
268 dimensional variance analysis proved to be effective in preventing artifacts caused by
269 uneven florescent intensity and lack of accumulation. At the same time, background
270 stochastic noise was significantly reduced because of the high degree of randomness of
271 the gradient vector. High-density STORM data that was processed using the gmSRRF
272 algorithm had fewer artifacts and less background noise. Widefield and confocal images
273 presented finer and more definite structures after processing. SIM, combined with the
274 gmSRRF algorithm, also produced fewer artifacts and balanced images. Overall, the
275 experimental results verified that the gmSRRF algorithm delivered a comprehensive
276 improvement in terms of artifacts compared to the SRRF algorithm for high-density
277 blinking, widefield, confocal fluctuating, and SIM data.

278

279 **Methods**

280 **Cell culture and transfection.** BS-C-1 cells obtained from the BeNa Collection in
281 China were cultured in Modified Eagle Medium (MEM) (Gibco), supplemented with
282 10% (v/v) FBS (Gibco), 100 units/mL penicillin-streptomycin (Gibco), and 1X MEM
283 non-essential amino acids (Gibco). Nearly 48 h after transfection with Lipofectamine
284 2000 (Invitrogen) and Opti-MEM (Life Technologies), cells were suspended and
285 seeded on the poly-l-lysine-coated 0.13–0.16 mm cover glass (Diamond) on the day
286 before fixation, and incubated at 37 °C with 5% CO₂.

287

288 **Cell fixing and staining.** Before imaging, cells were washed in phosphate buffered
289 saline (PBS) and fixed in 4% (w/v) paraformaldehyde (Electron Microscopy Sciences)
290 and 0.2% (w/v) glutaraldehyde (Life Science) for 15 min. For microtubule
291 immunolabeling, cells were treated with an extracting buffer (0.1 M PIPES, 1mM
292 EGTA, 1 mM MgCl₂, and 0.2% Triton X-100) for 1 min before fixation. After fixing,
293 the cells were reduced with 10 mM sodium borohydride (Sigma-Aldrich) for 5 min,
294 and permeabilized with 0.5% Triton X-100 (Sangon) for an additional 5 min. The cells
295 were washed again with PBS and treated with a blocking buffer containing 5% (w/v)
296 bovine serum albumin (Jackson ImmunoResearch Laboratories) and 0.5% Triton X-
297 100 in PBS for 30 min. For microtubule immunolabeling, mouse anti-alpha tubulin
298 (ab74696, Abcam) was used as the primary antibody in 1% BSA for 1 h, then anti-
299 mouse Alexa 488 (ab150113, Abcam) was used as a secondary antibody in 1% BSA for
300 an additional 1 h after washing 3 times. After staining, the specimens were mounted in
301 ProLong Glass Antifade Mountant (Invitrogen, Thermo Fisher Scientific). All the
302 above-mentioned operations were conducted at room temperature.

303

304 **Simulations.** All simulated data in Fig. 2 were generated using a Gaussian PSF profile
305 with a standard deviation of 200 nm. The maximum brightness of all fluorophores was
306 equal, and the fluctuation function $f_i(t)$ was a random sequence ranging between 0 and
307 1. The intensity distribution was pixelated at a pixel size of 30 nm. Specifically, the
308 profiles shown in Fig. 2a were produced through iteration. A new intensity distribution

309 was repeatedly generated and added to the previous sequence to produce a new value
310 of the weighting function until it converged to a steady state. The maximum relative
311 error of five consecutive values of the weighting function was less than 10^{-5} .

312

313 **Data analysis.** All data images were acquired in or converted to tiff format. The
314 variance analysis programs were written in MATLAB 2020a. The ImageJ plugin
315 ‘NanoJ SRRF’ (version 1.1Stable0) was used.

316

317 **Variance Analysis.** The first step of gmSRRF is variance analysis. Variance analysis
318 was written using a MATLAB script (Varana_21w17a.m, hereinafter referred to as
319 Varana). The Varana script conducts variance analysis and reweights the raw image
320 stack. Compared with the original weighting function $W(\mathbf{r})$, the Varana script adds some
321 details to prevent the potential issue of convergence, and is then compiled into three
322 MATLAB function files.

323 Ideally, the weighting function will converge to a minor value or zero in non-central
324 areas. However, the focal plane is mixed with the blurred images of defocused
325 structures due to the limitation of axial resolution. Therefore, the background offset
326 appeared to be uneven. The denser the cell structures, the stronger the background. In
327 these areas, the intensity variance tends to be high, while the gradient variance is the
328 opposite because of the integral fluorescent fluctuations. Consequently, a bright
329 background will cause misinterpretation of the cell structures. In any case, background
330 fluctuation is a smooth variation in a large spatial region. Varana used an intensity

331 variance threshold to ensure the convergence of the weighting function. Intensity
332 variance was believed to originate from fluctuations in fluorophores only when it
333 exceeded the threshold. The weighting function degenerated from $D[I(\mathbf{r})]/D[G(\mathbf{r})]$ to
334 $D[I(\mathbf{r})]$ when the intensity variance decreased below the threshold.

335

336 **SRRF analysis.** The basic settings were as follows: ring radius = 0.5, magnification =
337 6 or 3 (gmSRRF), and axes in ring = 6. Advanced settings were default values except
338 for the temporal analysis, which was the temporal radially average.

339

340 **References**

- 341 1. Moerner, W. E. & Kador, L. Optical detection and spectroscopy of single molecules in a solid.
342 *Phys. Rev. Lett.* **62** (21), 2535-2538 (1989). 10.1103/PhysRevLett.62.2535, Pubmed:10040013
- 343 2. Rust, M. J., Bates, M. & Zhuang, X. Sub-diffraction-limit imaging by stochastic optical
344 reconstruction microscopy (STORM). *Nat. Methods* **3** (10), 793-795 (2006). 10.1038/nmeth929,
345 Pubmed:16896339
- 346 3. Huang, B., Wang, W., Bates, M. & Zhuang, X. Three-dimensional super-resolution imaging by
347 stochastic optical reconstruction microscopy. *Science* **319** (5864), 810-813 (2008).
348 10.1126/science.1153529, Pubmed:18174397
- 349 4. Betzig, E. *et al.* Imaging intracellular fluorescent proteins at nanometer resolution. *Science* **313**
350 (5793), 1642-1645 (2006). 10.1126/science.1127344, Pubmed:16902090
- 351 5. Hess, S. T., Girirajan, T. P. & Mason, M. D. Ultra-high resolution imaging by fluorescence
352 photoactivation localization microscopy. *Biophys. J.* **91** (11), 4258-4272 (2006).
353 10.1529/biophysj.106.091116, Pubmed:16980368
- 354 6. Hell, S. W. & Wichmann, J. Breaking the diffraction resolution limit by stimulated emission:
355 stimulated-emission-depletion fluorescence microscopy. *Opt. Lett.* **19** (11), 780-782 (1994).
356 10.1364/ol.19.000780, Pubmed:19844443
- 357 7. Klar, T. A., Engel, E. & Hell, S. W. Breaking Abbe's diffraction resolution limit in fluorescence
358 microscopy with stimulated emission depletion beams of various shapes. *Phys. Rev. E Stat.*
359 *Nonlin. Soft Matter Phys.* **64** (6 Pt 2), 066613 (2001). 10.1103/PhysRevE.64.066613,
360 Pubmed:11736302
- 361 8. Gustafsson, M. G. Surpassing the lateral resolution limit by a factor of two using structured
362 illumination microscopy. *J. Microsc.* **198** (2), 82-87 (2000). 10.1046/j.1365-2818.2000.00710.x,
363 Pubmed:10810003
- 364 9. Lal, A., Shan, C. Y. & Xi, P. Structured Illumination Microscopy Image Reconstruction
365 Algorithm. *Ieee J Sel Top Quant* **22** (4), 50-63 (2016). 10.1109/JSTQE.2016.2521542
- 366 10. Tu, S. *et al.* Fast reconstruction algorithm for structured illumination microscopy. *Opt. Lett.* **45**

- 367 (6), 1567-1570 (2020). 10.1364/OL.387888, Pubmed:32164018
- 368 11. Huang, X. *et al.* Fast, long-term, super-resolution imaging with Hessian structured illumination
369 microscopy. *Nat. Biotechnol.* **36** (5), 451-459 (2018). 10.1038/nbt.4115, Pubmed:29644998
- 370 12. Westphal, V. *et al.* Video-rate far-field optical nanoscopy dissects synaptic vesicle movement.
371 *Science* **320** (5873), 246-249 (2008). 10.1126/science.1154228, Pubmed:18292304
- 372 13. Bergermann, F. *et al.* 2000-fold parallelized dual-color STED fluorescence nanoscopy. *Opt.*
373 *Express* **23** (1), 211-223 (2015). 10.1364/OE.23.000211, Pubmed:25835668
- 374 14. Cox, S. *et al.* Bayesian localization microscopy reveals nanoscale podosome dynamics. *Nat.*
375 *Methods* **9** (2), 195-200 (2011). 10.1038/nmeth.1812, Pubmed:22138825
- 376 15. Dertinger, T. *et al.* Fast, background-free, 3D super-resolution optical fluctuation imaging
377 (SOFI). *Proc. Natl Acad. Sci. USA* **106** (52), 22287-22292 (2009). 10.1073/pnas.0907866106,
378 Pubmed:20018714
- 379 16. Gustafsson, N. *et al.* Fast live-cell conventional fluorophore nanoscopy with ImageJ through
380 super-resolution radial fluctuations. *Nat. Commun.* **7**, 12471 (2016). 10.1038/ncomms12471,
381 Pubmed:27514992
- 382 17. Culley, S., Tosheva, K. L., Matos Pereira, P. & Henriques, R. SRRF: Universal live-cell super-
383 resolution microscopy. *Int. J. Biochem. Cell Biol.* **101**, 74-79 (2018).
384 10.1016/j.biocel.2018.05.014, Pubmed:29852248
- 385 18. Laine, R. F. *et al.* NanoJ: a high-performance open-source super-resolution microscopy toolbox.
386 *J. Phys. D Appl. Phys.* **52** (16), 163001 (2019). 10.1088/1361-6463/ab0261, Pubmed:33191949
- 387 19. Geissbuehler, S., Dellagiacom, C. & Lasser, T. Comparison between SOFI and STORM.
388 *Biomed. Opt. Express* **2** (3), 408-420 (2011). 10.1364/BOE.2.000408, Pubmed:21412447
- 389 20. Ovesný, M. *et al.* ThunderSTORM: a comprehensive ImageJ plug-in for PALM and STORM
390 data analysis and super-resolution imaging. *Bioinformatics* **30** (16), 2389-2390 (2014).
391 10.1093/bioinformatics/btu202, Pubmed:24771516
- 392 21. Dertinger, T. *et al.* Achieving increased resolution and more pixels with Superresolution Optical
393 Fluctuation Imaging (SOFI). *Opt. Express* **18** (18), 18875-18885 (2010).
394 10.1364/OE.18.018875, Pubmed:20940780
- 395 22. Biomedical Imaging Group. Benchmarking of single-molecule localization microscopy
396 software (Lausanne: EPFL, 2015), Available from: <http://bigwww.epfl.ch/smlm/>
- 397 23. Huff, J. The Airyscan detector from ZEISS: confocal imaging with improved signal-to-noise
398 ratio and super-resolution. *Nat. Methods* **12** (12), i-ii (2015). 10.1038/nmeth.f.388
- 399 24. Han, Y. *et al.* Ultra-fast, universal super-resolution radial fluctuations (SRRF) algorithm for
400 live-cell super-resolution microscopy. *Opt. Express* **27** (26), 38337-38348 (2019).
401 10.1364/OE.27.038337, Pubmed:31878602
- 402 25. Tescher, A. G., Klíma, M., Pospíšil, J. & Fliegel, K. *Applications of Digital Image Processing*
403 *XL*, 2017
- 404 26. Demmerle, J. *et al.* Strategic and practical guidelines for successful structured illumination
405 microscopy. *Nat. Protoc.* **12** (5), 988-1010 (2017). 10.1038/nprot.2017.019, Pubmed:28406496
- 406 27. Wen, G. *et al.* High-fidelity structured illumination microscopy by point-spread-function
407 engineering. *Light Sci. Appl.* **10** (1), 70 (2021). 10.1038/s41377-021-00513-w,
408 Pubmed:33795640
- 409 28. Fan, J. *et al.* A protocol for structured illumination microscopy with minimal reconstruction
410 artifacts. *Biophys. Rep.* **5** (2), 80-90 (2019). 10.1007/s41048-019-0081-7

411 **Acknowledgements**

412 This work was financially supported by the Ministry of science and technology of the
413 People's Republic of China (China-Serbia bilateral project SINO-SERBIA2018002),
414 Pioneering Project of Academy for Engineering and Technology, Fudan University
415 (gyy2018-001, gyy2018-002), Shanghai Natural Science Foundation (grant No.
416 20ZR1405100, 20ZR1403700), Science and Technology Research Program of
417 Shanghai (grant No. 19DZ2282100), Shanghai key discipline construction plan (2020-
418 2022) (grant No. GWV-10.1-XK01), Shanghai Engineering Technology Research
419 Center of Hair Medicine (19DZ2250500), China Postdoctoral Science Foundation
420 (2021M691089).

421 **Author contributions**

422 J.M. and B.W. conceived the project. B.W. and J.M. designed the experiments and
423 managed the project, L.Zh. prepared the biological cell specimens, L.Y., L.Zh. and L.Ch.
424 provided the plasmid construct of EGFP-Tubulin; X.G. and L.Zh. performed the
425 imaging experiment, X.G. and B.W. conducted the theoretical simulation and data
426 analysis with contributions from J.M., and L.M., X.G., L.Zh., B.W., and J.M. wrote the
427 manuscript. All authors discussed the results and manuscript.

428 **Additional information**

429 Supplementary Information accompanies this paper.

430 **Conflicts of interest**

431 There are no conflicts to declare.

Supplementary Files

This is a list of supplementary files associated with this preprint. Click to download.

- [Varanasourcecode.zip](#)
- [Supplementaryinformation.pdf](#)